INTERNATIONAL JOURNAL FOR NUMERICAL METHODS IN FLUIDS
Int. J. Numer. Meth. Fluids 2009; **59**:927–943
Published online 9 July 2008 in Wiley InterScience (www.interscience.wiley.com). DOI: 10.1002/fld.1855

Three-dimensional numerical simulation of compound meandering open channel flow by the Reynolds stress model

H. Jing[1,*,†], Y. Guo[2], C. Li[1] and J. Zhang[2]

[1]*Research Institute of Numerical Computation and Engineering Applications, North University for Ethnics, Yinchuan, Ningxia 750021, China*
[2]*Department of Engineering, University of Aberdeen, Aberdeen, Scotland AB24 3UE, U.K.*

SUMMARY

Turbulent flow in a compound meandering open channel with seminatural cross sections is one of the most complicated turbulent flows as the flow pattern is influenced by the combined action of various forces, such as centrifugal force, pressure, and shear stresses. In this paper, a three-dimensional (3D) Reynolds stress model (RSM) is adopted to simulate the compound meandering channel flows. Governing equations of the flow are solved numerically with finite-volume method. The velocity fields, wall shear stresses, and Reynolds stresses are calculated for a range of input conditions. Good agreement between the simulated results and measurements indicates that RSM can successfully predict the complicated flow phenomenon. Copyright © 2008 John Wiley & Sons, Ltd.

Received 29 January 2008; Revised 18 April 2008; Accepted 4 May 2008

KEY WORDS: Reynolds stress model; turbulent flow; compound meandering channel; numerical simulation; open channel flow; wall shear stress

1. INTRODUCTION

Secondary currents are generated in open channel flows because free surface and walls reduce the turbulence intensity in the direction normal to the surface or the walls and lead to anisotropy

*Correspondence to: H. Jing, Research Institute of Numerical Computation and Engineering Applications, North University for Ethnics, Yinchuan, Ningxia 750021, China.
†E-mail: jinghef@163.com

Contract/grant sponsor: National Natural Science Foundation of China; contract/grant number: 10671157
Contract/grant sponsor: Natural Science Foundations of Ningxia, China; contract/grant number: 2006241
Contract/grant sponsor: Institutions of Higher Educations of Ningxia; contract/grant number: 2006JY016
Contract/grant sponsor: Ministry of Education of China
Contract/grant sponsor: University of Aberdeen

Copyright © 2008 John Wiley & Sons, Ltd.

of turbulence. For straight open channel flows, though the magnitude of the secondary currents is only about 2% of the maximum primary flow velocity [1], they have a certain effect on the mean flow and turbulence structures. For compound meandering channel flows, the secondary currents play a much more important role. In the past three decades, the flow in straight and compound meandering open channels has been extensively studied, both numerically and experimentally, to understand the turbulent flow behavior and to predict the conveyance capacity. Various numerical models, such as standard k–ε model [2], nonlinear k–ε model [3], algebraic Reynolds stress model (ASM) [4], Reynolds stress model (RSM) [1], and large eddy simulation (LES) [5], have been developed to simulate the turbulent structure in compound meandering open channel. The standard k–ε model is an isotropic turbulence closure and cannot reproduce the secondary flows [6, 7]. Although nonlinear k–ε model can simulate secondary currents successfully in a compound channel, it cannot accurately capture some of the turbulence structures [8]. The ASM is economical because it simplified the Reynolds stress transport equations by replacing them with algebraic equations. However, Reference [9] indicates that the accuracy of the mean flow and turbulence structures simulated using this model (ASM) are poor. The RSM computes the Reynolds stress by solving the Reynolds stress transport equations directly, but its application to open channel flows is still limited due to the complexity of the model. Kang and Choi [1] using RSM simulated a straight open channel flow and obtained some useful results. To the best of the authors' knowledge, three-dimensional (3D) numerical simulations of compound meandering open channel flows with seminatural cross sections using RSM have not been reported.

In contrast to straight channel flow, fewer studies have been carried out on turbulent flow in compound meandering channels, which generate much more complex flow. The flow pattern in such compound meandering channels is affected by various forces, such as centrifugal forces, pressure-driven forces, and shear stresses generated by momentum transfer between the main channel and the flood plain [10]. Owing to its practical importance and theoretical interests, compound meandering open channel flows have been extensively studied, primarily through laboratory experiments [11–17]. In particular, the series experiments performed using U.K. Flood Channel Facility (U.K.-FCF) [15] greatly improved our knowledge and understanding of flow characteristics in compound meandering channels.

In this study, RSM is adopted to simulate the turbulent flow in meandering compound channel, which is highly 3D and has strong secondary currents. Taking 60° compound meandering channel [15] as an example, the authors find that the RSM can accurately simulate the distribution of tangential velocity, transverse velocity, wall shear stresses, and Reynolds stresses. Four cases (one being inbank flow and other three being overbank flow) with different water depths were calculated. The results show both water depth and average velocity in main channel have significant effects on the magnitude and direction of secondary currents, and wall shear stresses. Given that the natural rivers are generally meandering, the study has immediate practical importance and engineering application.

2. NUMERICAL MODEL

The governing equations in the RSM are Reynolds-averaged continuity and momentum equations, Reynolds stress transport equations, and transport equation of kinetic energy's dissipation rate. For

Copyright © 2008 John Wiley & Sons, Ltd.

DOI: 10.1002/fld

fully developed turbulent flow, the Reynolds time-averaged continuity and momentum equations are

$$\frac{\partial \overline{u}_i}{\partial x_i} = 0 \tag{1}$$

$$\overline{u}_j \frac{\partial \overline{u}_i}{\partial x_j} = -\frac{1}{\rho}\frac{\partial \overline{p}}{\partial x_i} + \frac{\partial}{\partial x_j}\left(v\frac{\partial \overline{u}_i}{\partial x_j} - \overline{u_i' u_j'}\right) + g_i, \quad i = 1, 2, 3 \tag{2}$$

where x_1, x_2, and x_3 are the longitudinal, lateral, and vertical directions; $\overline{u}_i$ is the Reynolds time-averaged velocity in the x_i direction, $i = 1, 2, 3$; $\overline{p}$ is the Reynolds time-averaged pressure; v is the kinematic viscosity; ρ is the density of water; $g_1 = g_2 = 0$, $g_3 = -g$ and g is the gravitational acceleration; $\overline{u_i u_j}$ $(i, j = 1, 2, 3)$ is the Reynolds stress R_{ij}, which can be obtained by solving the Reynolds stress transport equations:

$$\overline{u}_l \frac{\partial R_{ij}}{\partial x_l} = -\left(R_{il}\frac{\partial \overline{u}_j}{\partial x_l} + R_{jl}\frac{\partial \overline{u}_i}{\partial x_l}\right) + D_{ij} - \varepsilon_{ij} + \Pi_{ij} \tag{3}$$

where D_{ij} is the transport of R_{ij} $(i = 1, 2, 3)$ by diffusion and can be determined by [18]

$$D_{ij} = C_s \frac{\partial}{\partial x_l}\left[\frac{k^2}{\varepsilon}\left(\frac{\partial R_{ij}}{\partial x_l} + \frac{\partial R_{il}}{\partial x_j} + \frac{\partial R_{jl}}{\partial x_i}\right)\right] \tag{4}$$

in which C_s is a constant $(= 0.22/3)$, and $k = R_{ii}/2$ is the turbulent kinetic energy. The dissipation rate of R_{ij} is

$$\varepsilon_{ij} = \tfrac{2}{3}\varepsilon\delta_{ij} \tag{5}$$

where ε is the dissipation rate of k and δ_{ij} Kronecker's delta. ε can be obtained by the following equation:

$$\overline{u}_j \frac{\partial \varepsilon}{\partial x_j} = \frac{\partial}{\partial x_m}\left(C_\varepsilon \frac{k}{\varepsilon} R_{ml}\frac{\partial \varepsilon}{\partial x_l}\right) + \frac{\varepsilon}{k}\left(C_{\varepsilon 1} P_k - C_{\varepsilon 2}\varepsilon\right) \tag{6}$$

where P_k is the rate of production of turbulence kinetic energy with $C_\varepsilon = 0.18$, $C_{\varepsilon 1} = 1.45$, $C_{\varepsilon 2} = 1.90$. The last term in Equation (3) is the pressure–strain term, which acts to redistribute turbulent kinetic energy among the Reynolds stresses and can be determined by [19]

$$\begin{aligned}\Pi_{ij} = {} & \alpha_0 \varepsilon b_{ij} + \alpha_1 \varepsilon\left(b_{im}b_{jm} - \tfrac{1}{3}b_{mn}b_{nm}\delta_{ij}\right) + \alpha_2 k S_{ij} \\ & + \alpha_3 P_k b_{ij} + \alpha_4 k\left(b_{im}S_{jm} + b_{jm}S_{im} - \tfrac{2}{3}b_{ml}S_{ml}\delta_{ij}\right) \\ & + \alpha_5 k\left(b_{im}W_{jm} + b_{jm}W_{im}\right)\end{aligned} \tag{7}$$

in which b_{ij} $(= R_{ij}/2k - \frac{1}{3}\delta_{ij})$ is the anisotropy tensor, S_{ij} $(= \frac{1}{2}(\partial \overline{u}_i/\partial x_j + \partial \overline{u}_j/\partial x_i))$ the rate of the strain tensor, W_{ij} $(= \frac{1}{2}(\partial \overline{u}_i/\partial x_j - \partial \overline{u}_j/\partial x_i))$ the rotation tensor, and $\alpha_0 = -3.4$, $\alpha_1 = 4.2$, $\alpha_2 = 0.8 - 1.3(b_{ij}b_{ji})^{1/2}$, $\alpha_3 = -1.8$, $\alpha_4 = 1.25$, and $\alpha_5 = 0.4$. The finite-volume method is applied to discretize the governing equations. The staggered grid system is used for spatial discretization of governing equations. The SIMPLEC algorithm is adopted to treat the pressure–velocity coupling [20]. The discretization equations are solved using the general TDMA method [21].

Copyright © 2008 John Wiley & Sons, Ltd.

DOI: 10.1002/fld

3. DESCRIPTION OF NUMERICAL EXAMPLE—THE 60° COMPOUND MEANDERING CHANNEL

The U.K.-FCF was a large flume, which was 50 m long and 10 m wide, and had a discharge capacity of 1.1 m^3/s. One of the three channels, the 60° meandering channel was considered in this study. Initially, the main channel was constructed with a prismatic trapezoidal section and a 45° bank slope. The main channel was 0.15 m deep with top width of 1.2 m. The flood plains were on the slope of 9.96×10^{-4}. One wavelength of the meander was 12.0 m. Then the main channel was modified to a seminatural geometry, in which the cross section changed throughout the meander wavelength in accordance with known geomorphologic principles. Figure 1 is the sketch of 3D geometry of the compound meandering channel in one wavelength. Figure 2 shows the plain view and the arrangement of the cross sections where the measurements were taken. Figure 3 shows cross section geometry of the channel.

The dimensions ($b1$–$b6$) of cross sections displayed in Figure 3 for the 60° meandering channel are given in Table I. The angles of these cross sections are shown in Figure 2, in which the angle

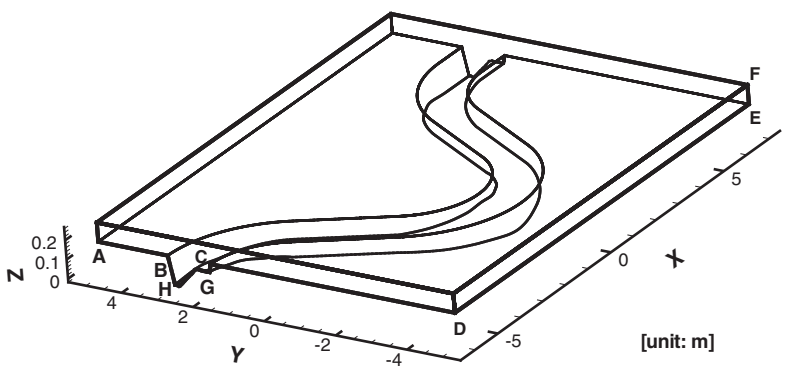

Figure 1. Sketch of 3D configuration of the channel.

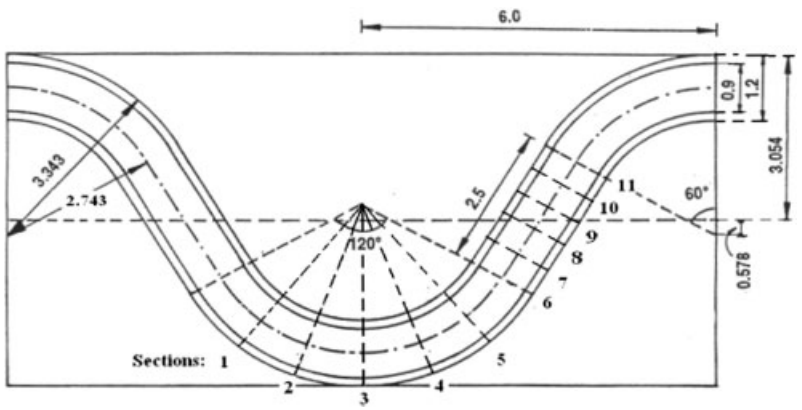

Figure 2. Plane view of one wavelength of the channel (unit: m).

Copyright © 2008 John Wiley & Sons, Ltd.

DOI: 10.1002/fld

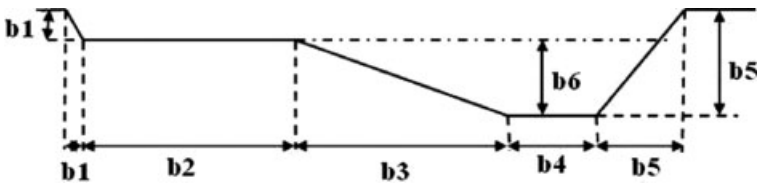

Figure 3. Sketch of side view of the cross section of channel.

Table I. Size for typical cross sections of the channel (angle unit: degree; length unit: m).

Angle	$b1$	$b2$	$b3$	$b4$	$b5$	$b6$
0	0.045	0.375	0.480	0.150	0.150	0.105
12	0.054	0.406	0.362	0.245	0.133	0.079
20	0.060	0.427	0.294	0.295	0.124	0.064
24	0.063	0.436	0.262	0.317	0.120	0.057
36	0.072	0.469	0.167	0.384	0.108	0.036
40	0.074	0.480	0.140	0.401	0.105	0.031
48	0.080	0.501	0.081	0.440	0.098	0.018
60	0.089	0.532	0.000	0.489	0.089	0.0

of Section 3 was defined as 0°. The geometry of cross section is symmetric about Section 3 with a straight channel connecting Sections 6 and 11. More details about U.K.-FCF and experiments can be found in [15–17].

4. BOUNDARY CONDITIONS

4.1. Wall boundary

The non-slip boundary condition is applied on all walls. The standard wall-function law is used to estimate the velocity parallel to the channel bed at the first cell and is expressed as [22]

$$U^* = \frac{1}{\kappa}\ln(Ey^*) \tag{8}$$

with

$$U^* = \frac{u_P C_\mu^{0.25} k_P^{0.5}}{\tau_w/\rho}, \quad y^* = \frac{\rho C_\mu^{0.25} k_P^{0.5} y_P}{\mu} \tag{9}$$

where u_P is the mean velocity at near wall node P; U^* is the friction velocity; κ is the von Karman constant equal to 0.42; E is the roughness parameter equal to 9.793; C_μ is an empirical constant equal to 0.09; y_P is the distance of P to the solid wall; τ_w is wall shear stress; ρ is the density; k_P is turbulence kinetic energy at P; μ is dynamic viscosity; and v is the kinematic viscosity. The logarithmic law for mean velocity is employed when $y^* > 11.225$. When the mesh is such that $y^* < 11.225$ at the wall adjacent cells, the laminar stress–strain relationship is applied

Copyright © 2008 John Wiley & Sons, Ltd.

DOI: 10.1002/fld

that can be expressed as

$$U^* = y^* \tag{10}$$

Since local equilibrium is assumed in the vicinity of the wall, the dissipation rate is set equal to the production of k. For the Reynolds normal stresses at the wall, the zero gradient condition is used. The Reynolds shear stresses at the wall vicinity are set equal to the value from the logarithmic law.

4.2. Free surface

Rigid lid approximation is applied to the free surface in the simulation. At the free surface, the velocity components and turbulent kinetic energy are treated as a symmetry plane, while the dissipation rate is computed from the relationship given by Celik and Rodi [23]. It reduces the length scale of turbulence near the free surface

$$\varepsilon_f = \frac{k_f^{3/2}}{0.43 h_f} \tag{11}$$

where k_f is the value of k at the free surface and h_f is the free surface height from the bed.

4.3. Inlet and outlet boundaries

The average velocity at inlet is computed by $U_{in} = Q/A$, where Q is the flow discharge of the channel and A is the cross section area of the inlet. Turbulence kinetic energy k and its dissipation rate ε, u, v, w (velocities in the x, y, z directions and are initially assumed to be uniform at the inlet) at the inlet are calculated as

$$u = U_{in}, \quad v = 0, \quad w = 0, \quad k_{in} = \tfrac{3}{2}(I U_{in})^2, \quad \varepsilon_{in} = c_\mu^{3/4} \frac{k^{3/2}}{0.1R} \tag{12}$$

Table II. Input flow conditions at inlet.

	DR	Q (m^3/s)	H (m)	U_{in} (m/s)	k_{in} (m^2/s^2)	ε_{in} (m^2/s^3)
Case 1	0	0.03239	0.140	0.39	2.76×10^{-3}	1.275×10^{-4}
Case 2	0.0909	0.05821	0.165	0.24	8.46×10^{-4}	2.45×10^{-4}
Case 3	0.25	0.22236	0.20	0.38	2.1×10^{-3}	8.01×10^{-4}
Case 4	0.40	0.613	0.25	0.596	5.3×10^{-3}	2.6×10^{-3}

Table III. Summary of grid cells.

	AB	BC,HG	BH,GC	CD	DE	EF	Volume elements
Case 1 (DR = 0)	—	30	14	—	170	—	71 400
Case 2 (DR = 0.0909)	40	40	13	140	240	8	547 200
Case 3 (DR = 0.25)	40	40	15	140	320	10	896 000
Case 4 (DR = 0.40)	35	30	12	103	230	10	469 200

Copyright © 2008 John Wiley & Sons, Ltd.

DOI: 10.1002/fld

where I is turbulent intensity assumed to be 10% and R is the hydraulic radius at inlet. The Reynolds stresses at inlet can be calculated by

$$R_{11}=R_{22}=R_{33}=\tfrac{2}{3}k_{\text{in}},\quad R_{12}=R_{13}=R_{23}=0 \tag{13}$$

At the outlet, the pressure is set as zero on the free surface and the fully developed flow condition is applied, i.e.

$$\frac{\partial u}{\partial x}=\frac{\partial v}{\partial x}=\frac{\partial w}{\partial x}=\frac{\partial \varepsilon}{\partial x}=0,\quad \frac{\partial R_{ij}}{\partial x}=0,\quad i,j=1,2,3 \tag{14}$$

Because the cross section of the channel is strongly asymmetry and non-uniform, the use of cross section average velocity of the section as the inlet boundary condition may lead to large discrepancy between computed and measured results. In order to improve computational accuracy, the simulation is performed twice. The uniform velocity at the inlet is used in the first simulation. The simulated velocity at the outlet is used as input boundary condition at the inlet in the second simulation.

In order to investigate the flow behavior in meandering channels with seminatural cross sections, four cases of turbulent flow with various water depths are considered. Table II lists the input conditions at the inlet, where DR is the relative water depth, defined as $\text{DR}=h/H$ with h being water depth over the flood plain and H being maximum water depth of the main channel.

4.4. Meshes

Only one wavelength of the 60° compound meandering channel was considered in this study. The flow domain was discretized using structured grid and the body-fitted coordinates were used. Table III lists the numbers of grid cells of some edges shown in Figure 1 and the total numbers of volume elements for the four cases investigated in this paper.

5. RESULTS AND DISCUSSIONS

5.1. Turbulence properties

The turbulent flow properties, such as tangential velocity, transverse velocity, wall shear stress, and Reynolds shear stresses, are simulated for all four cases listed in Tables II and III. The simulation shows that the flow patterns are similar. Therefore, only the results for Case 3 are presented and discussed in this section.

Figure 4 shows the calculated and measured contours of tangential velocities of the meandering channel on Sections 1, 3, and 5. The direction of the tangential velocity is parallel to the tangent of the centerline of the meandering channel. The left-hand side of these cross sections is inner banks (looking downstream) and the right-hand side is outer banks.

Both calculated and measured results in Figure 4 demonstrate that the maximum tangential velocity that occurs near the inner bank of the main channel as the flow enters the curved part from straight reach. The maximum tangential velocity then gradually transfers from the inner bank to the outer bank as flow moves downstream.

It is seen that the numerical simulation is in reasonable agreement with the measurements. However, as shown in Figure 4, some deviations between measured and calculated results are

Copyright © 2008 John Wiley & Sons, Ltd.

DOI: 10.1002/fld

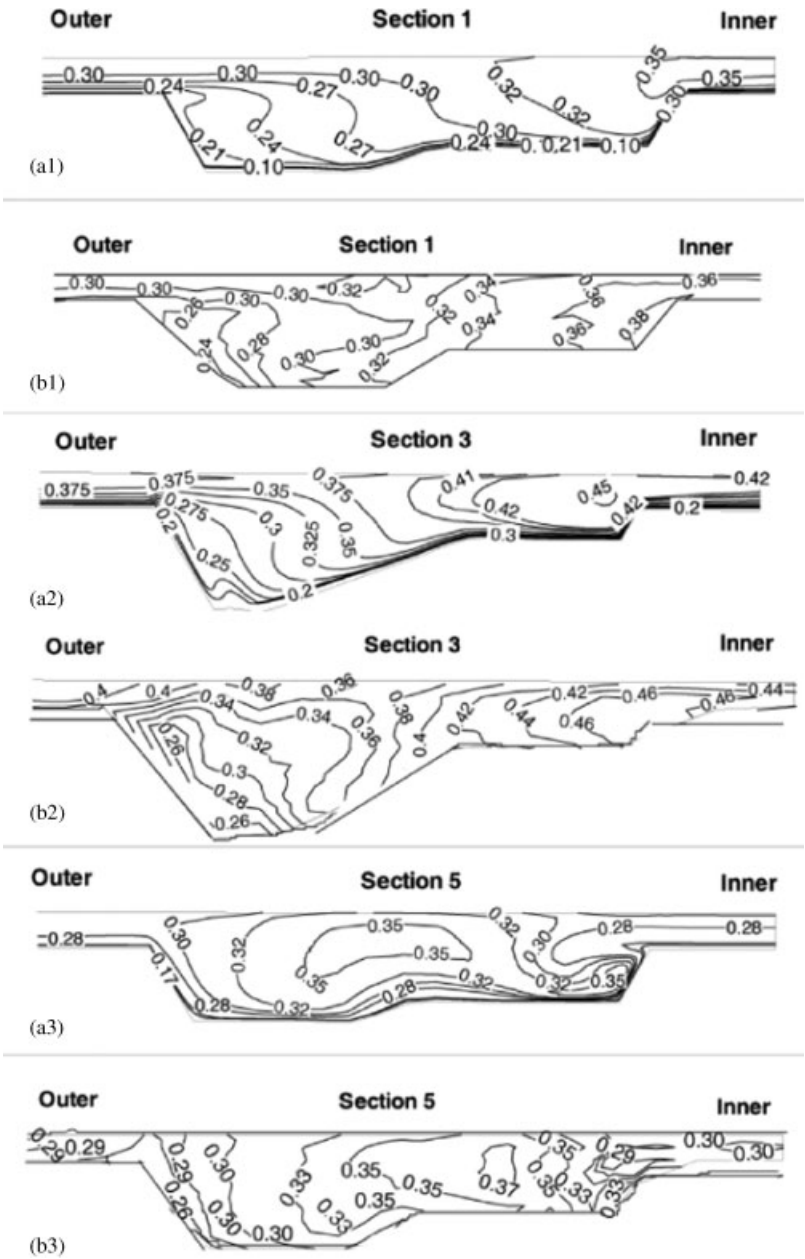

Figure 4. Comparison of calculated (*a*1, *a*2, and *a*3) and measured (*b*1, *b*2, and *b*3) tangential velocities on Sections 1, 3, and 5 (velocity unit: m/s).

Copyright © 2008 John Wiley & Sons, Ltd.

DOI: 10.1002/fld

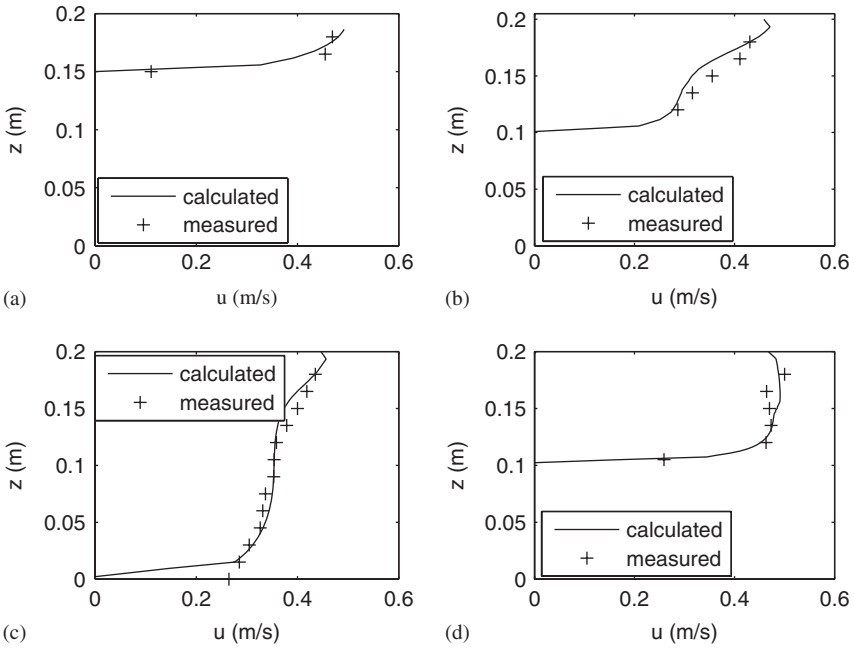

Figure 5. Vertical profiles of tangential velocity on Section 3 (z is the vertical coordinate and y is the transverse distance from the apex (m)): (a) $y=-0.3$ m; (b) $y=0.05$ m; (c) $y=0.25$ m; and (d) $y=0.75$ m.

found in some regions of the meandering channel, especially near the main channel–flood plain interaction regions. This deviation may be caused primarily by the large amount of momentum transportation between main channel and flood plain.

In order to make a clear comparison between measured and calculated velocity, four vertical profiles of tangential velocity on Section 3 for Case 3 are shown in Figure 5. Both the simulated and measured results show that the tangential velocity is predicted quite well in main channel where the channel bed has mild transverse gradient ($y=0.25$ m) and on the flood plain ($y=-0.3$ m). However, there existed some slight discrepancies between measured and calculated results in main channel–flood plain interaction regions ($y=0.05$ m) and in main channel where the channel bed has steeper transverse gradient ($y=0.75$ m).

Figure 6 is the comparison of calculated and measured transverse velocity fields at three cross sections. The positive value means that the flow direction is from the inner bank to the outer bank, while the negative velocity means that the flow moves in the opposite direction. It is seen that the configuration of the cross sections has a significant effect on the transverse velocity. The figure shows that the transverse flow at Section 1 is quite strong and complex with the flow near the surface moving towards the inner bank while the flow near the bed of the main channel moving towards the outer bank. As the flow reaches Section 3, transverse velocity weakens and has a turn of direction, namely, the flow near the surface/bed moves towards the outer bank/inner bank. Then transverse flow strengthens gradually after the flow passes through Section 3. However, for inbank flow in meandering channel, as can be seen in Figures 10–12, the transverse flow near the surface/bed always moves towards outer/inner bank on all cross sections. The results show that

Copyright © 2008 John Wiley & Sons, Ltd.

DOI: 10.1002/fld

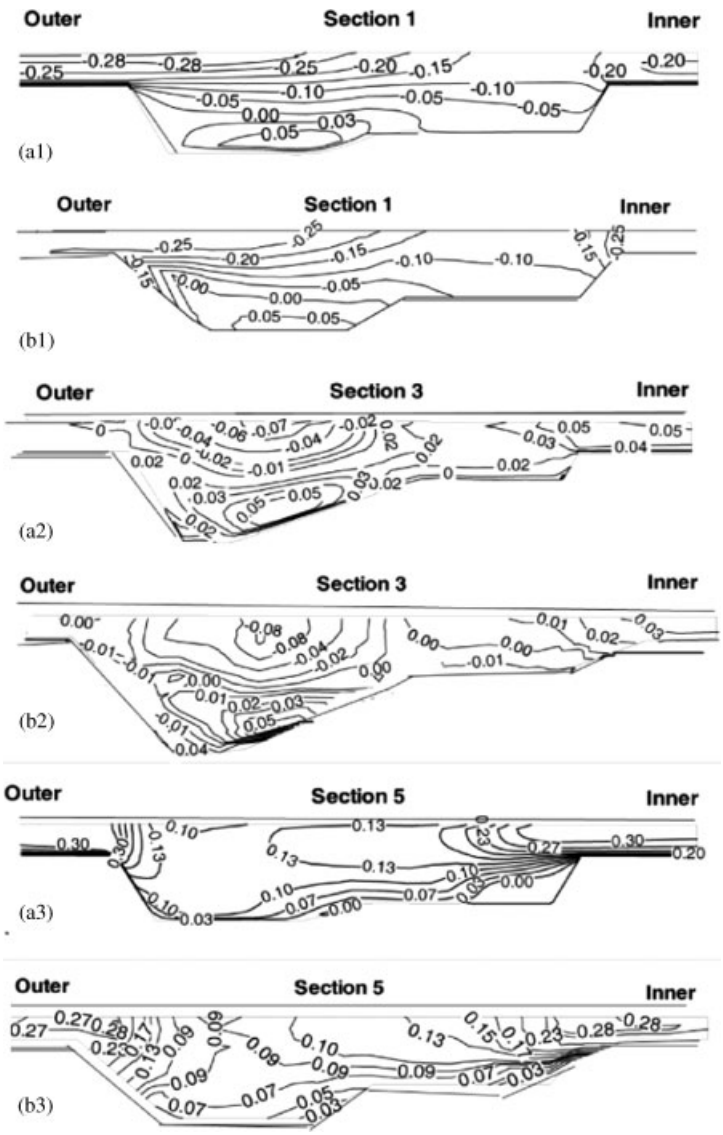

Figure 6. Comparison of calculated (*a*1, *a*2, and *a*3) and measured (*b*1, *b*2, and *b*3) transverse velocities on Sections 1, 3, and 5 (velocity unit: m/s).

the secondary flow direction of inbank flow is mainly affected by the centrifugal force. However, in the case of overbank flow in meandering channel, the secondary flow direction in main channel is affected not only by centrifugal force but also by interaction between the flow over flood plain and main channel flow.

By comparing the wall shear stress between calculated and measured results shown in Figure 7, it was concluded that the RSM can predict the wall shear stress with reasonable accuracy. Good agreement between the calculated and measured wall shear stresses was found in the main channel.

Copyright © 2008 John Wiley & Sons, Ltd.

DOI: 10.1002/fld

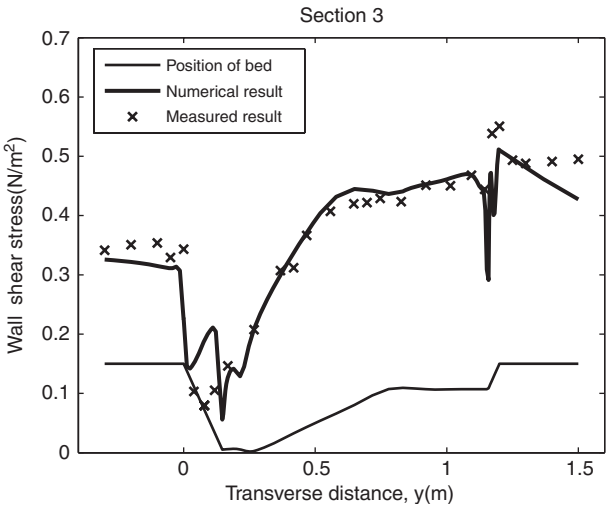

Figure 7. Comparison of calculated and measured wall shear stress on Section 3.

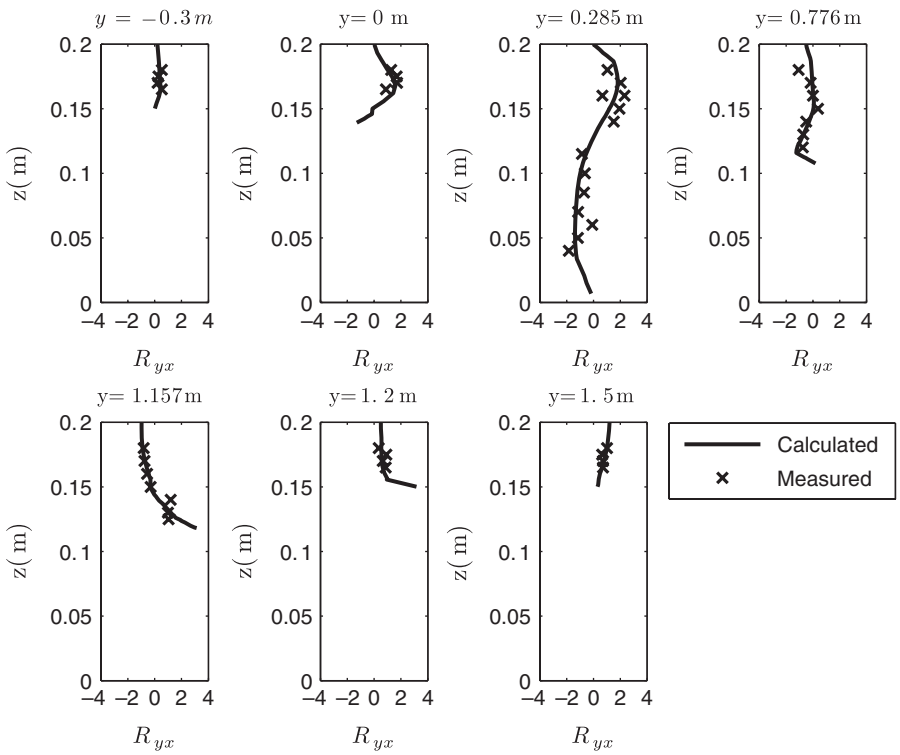

Figure 8. Vertical profiles of the Reynolds stress R_{yx} on Section 3 (y is the transverse distance from the apex (m), z is the vertical coordinate (m), and R_{yx} is the Reynolds stress ($10^{-4}\,\mathrm{m}^2/\mathrm{s}^2$)).

Copyright © 2008 John Wiley & Sons, Ltd.

DOI: 10.1002/fld

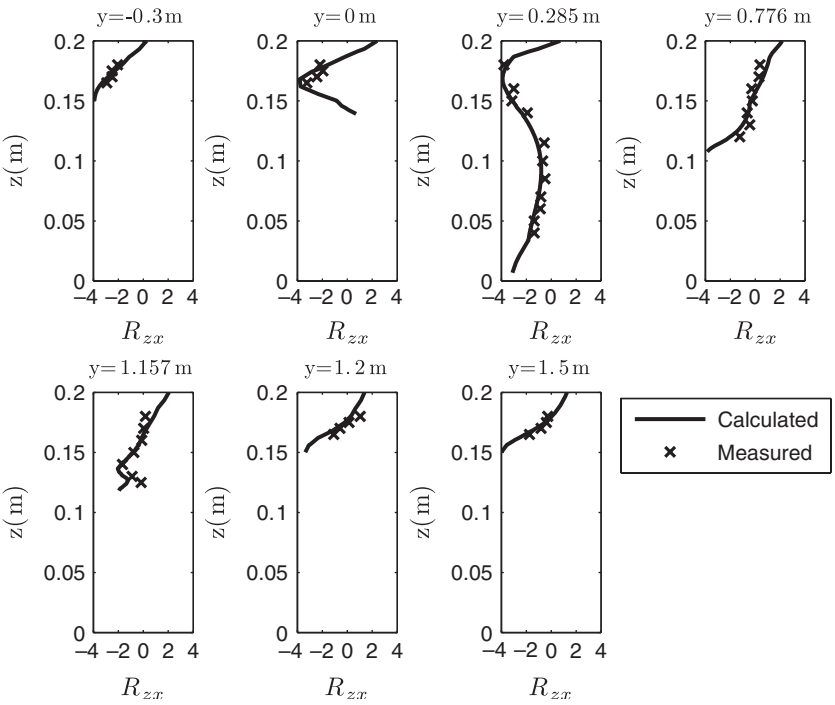

Figure 9. Vertical profiles of Reynolds stress R_{zx} on Section 3 (y is the transverse distance from the apex (m), z is the vertical coordinate (m), and R_{zx} is the Reynolds stress ($10^{-4}\,\mathrm{m}^2/\mathrm{s}^2$)).

Although the numerical model produced the wall shear stress that was similar to the tendency of the measurements, some discrepancy occurred in main channel corner regions and main channel–flood plain interaction regions. This deviation may be caused by the secondary flows affected primarily by the large amount of momentum transportation between main channel and flood plain. Figure 7 also shows that the minimum wall shear stress occurred at the junctions between the bed and the outer bank of main channel, whereas the maximum value was found to be at the junction between the main channel bank and the flood plain. The wall shear stress was usually larger near the inner bank than that near the outer bank.

Figures 8 and 9 are the calculated and measured Reynolds shear stresses R_{yx} and R_{zx} at seven typical perpendicular lines on Section 3. It is seen that the simulated results favorably compare with the measurements, indicating that the model can accurately predict Reynolds shear stresses (R_{yx} and R_{zx}). Small Reynolds shear stress R_{yx} takes place wherever the channel bed or flood plain has mild transverse gradient (see Figure 8, $y=-0.3$ and 1.5 m). Steeper transverse gradient (see rest of Figure 8) generates greater Reynolds shear stress R_{yx}. The reason is that flow velocity gradient with respect to the transverse direction is greater wherever the channel bed has steeper transverse gradient and *vice versa*.

For Reynolds shear stress R_{zx}, as shown in Figure 9, its absolute maximum value takes place near the channel solid wall, where larger gradient of main flow velocity with respect to the vertical direction occurs.

Copyright © 2008 John Wiley & Sons, Ltd.

DOI: 10.1002/fld

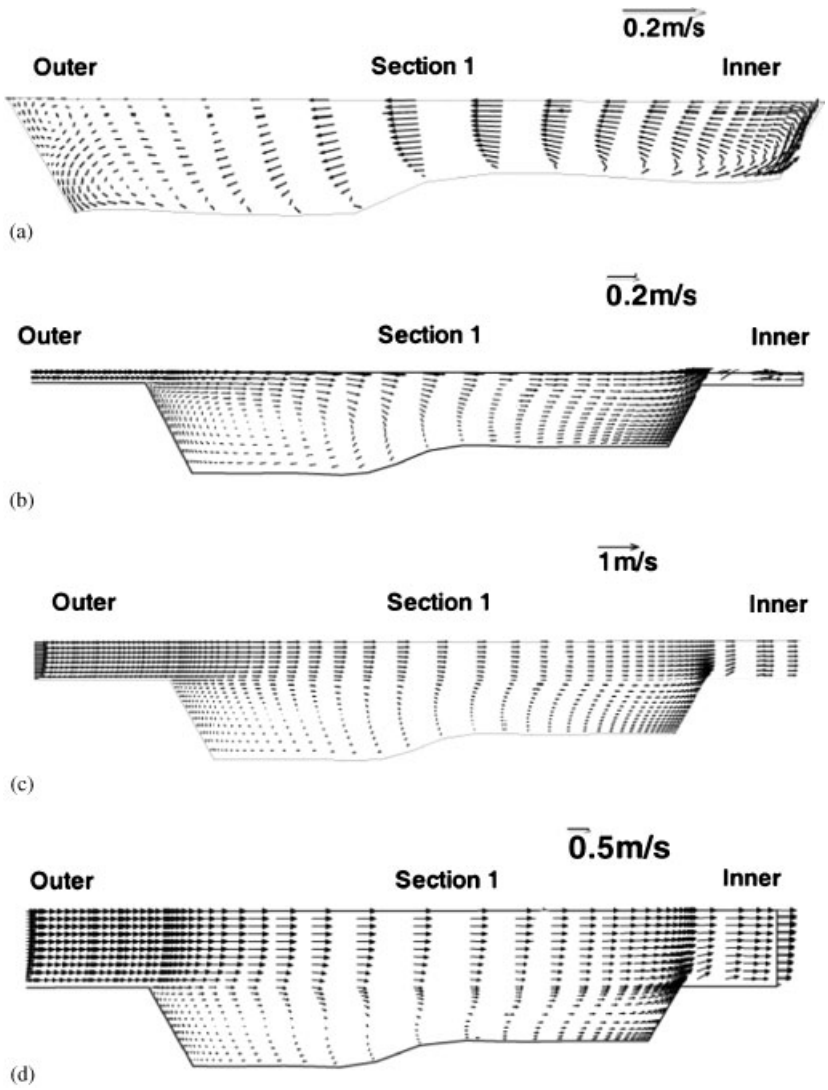

Figure 10. Comparison of secondary velocities of four cases on Section 1: (a) Case 1; (b) Case 2; (c) Case 3; and (d) Case 4.

5.2. *Effect of water depth*

Figures 10–12 are the calculated secondary flow fields on three cross sections for four cases. It is seen that the water depth has a significant influence on the secondary flow velocity. For the inbank flow case (Case 1), the directions of secondary currents near free surface in main channel are always towards the outer bank on Sections 1, 3, and 5, due to the centrifugal force. However, for the overbank flow cases (Cases 2–4), in addition to centrifugal force, the flow in

Copyright © 2008 John Wiley & Sons, Ltd.

DOI: 10.1002/fld

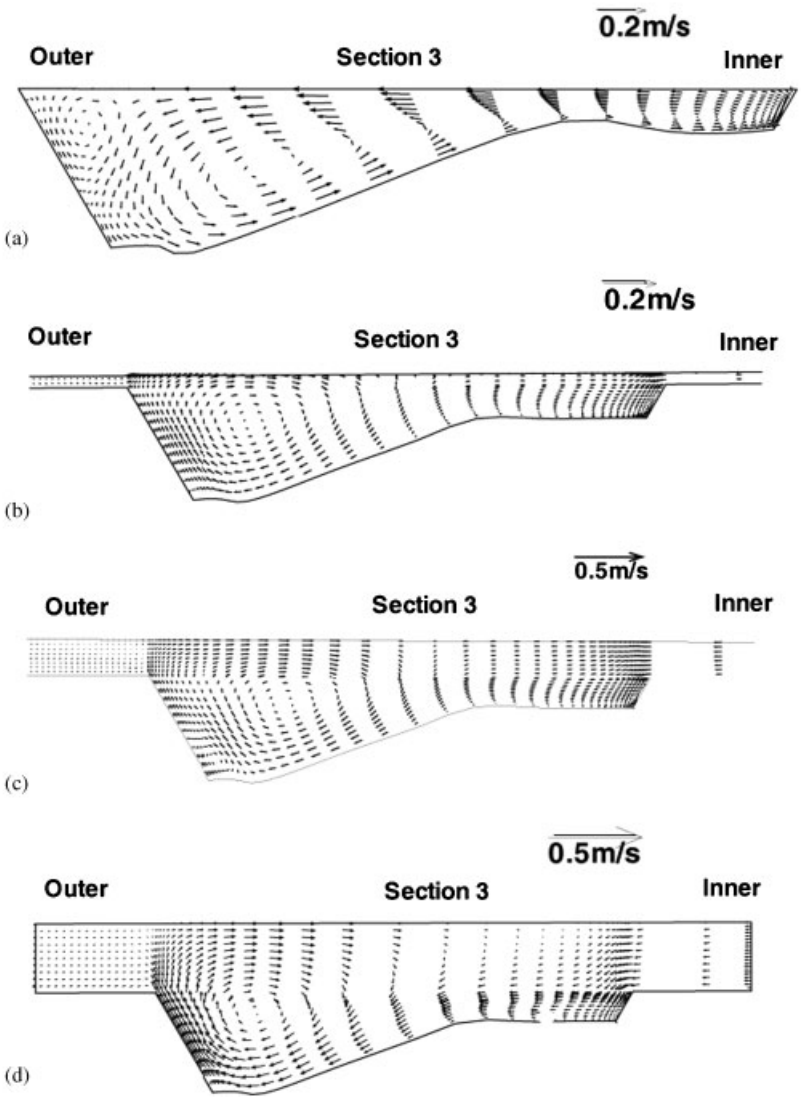

Figure 11. Comparison of secondary velocities of four cases on Section 3: (a) Case 1; (b) Case 2; (c) Case 3; and (d) Case 4.

main channel is also affected by the interaction between flows in main channel and over flood plain. As a result, the secondary currents near flood plain level are not necessarily towards the outer bank. On Sections 1 and 3, as shown in Figures 10 and 11, the secondary currents near flood plain level in main channel move towards inbank. However, on Section 5, as shown by Figure 12, they flow towards outer bank. Furthermore, secondary currents become stronger as water depth increases.

Copyright © 2008 John Wiley & Sons, Ltd.

DOI: 10.1002/fld

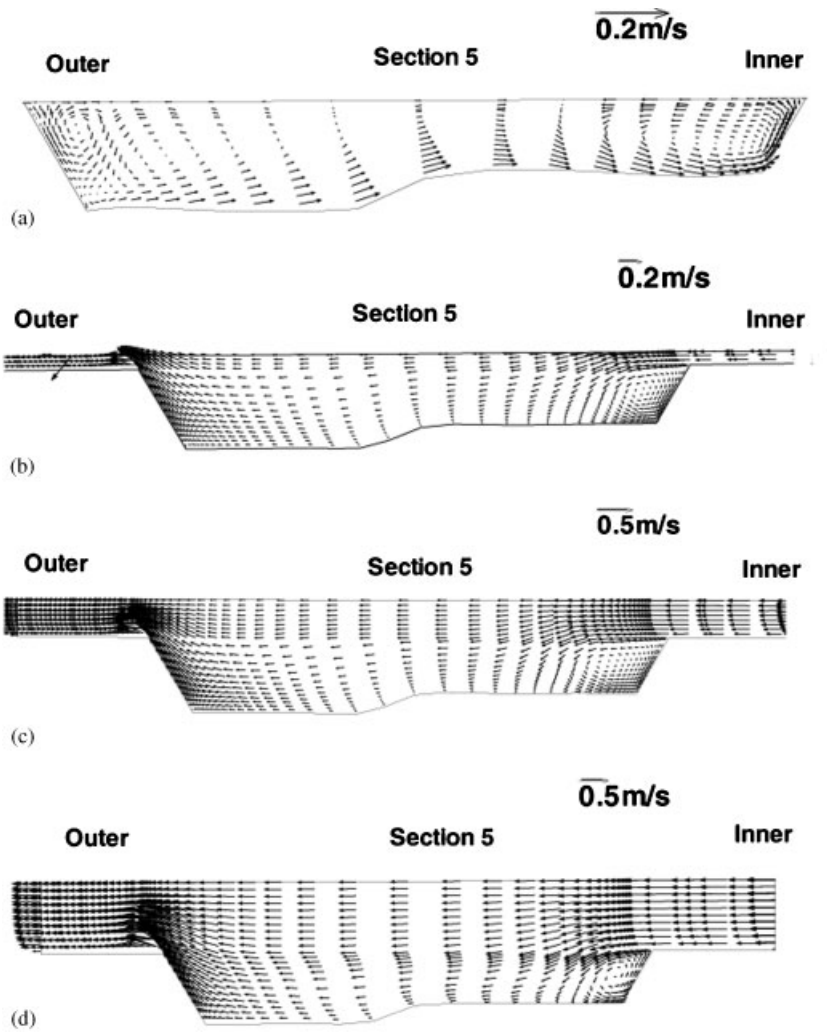

Figure 12. Comparison of secondary velocities of four cases on Section 5: (a) Case 1; (b) Case 2; (c) Case 3; and (d) Case 4.

Figure 13 is the simulated averaged wall shear stress. In general, the wall shear stress increases with the average velocity at inlet (see Table II). Owing to the large amount of momentum transportation between main channel and flood plain, large velocity gradient existed near the junctions between the main channel bank and the flood plain. As a result, the wall shear stress at these junctions was larger than other places.

By examining average velocity at inlet in Table II, it was shown that the average velocity for Case 2 was the smallest among the four cases and, in turn, the average wall shear stress of Case 2 on each of the three cross sections was also the smallest, as shown in Figure 13. On the contrary, for Case 4, the average wall shear stress was the largest as the largest average velocity used in this case.

Copyright © 2008 John Wiley & Sons, Ltd.

DOI: 10.1002/fld

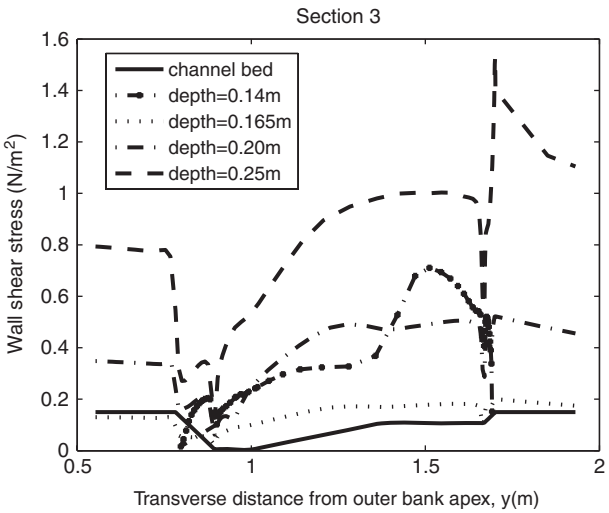

Figure 13. Comparison of wall shear stresses of four cases on Section 3.

6. CONCLUSIONS

A 3D numerical turbulence model was applied to simulate turbulent flows in a 60° compound meandering channel with seminatural cross sections. The velocity fields, wall shear stress, and Reynolds shear stresses were calculated for various input flow conditions. The simulated velocity fields and Reynolds shear stresses are in reasonable good agreement with the U.K.-FCF measurements. Effects of water depth on secondary flow and wall shear stress were also studied.

ACKNOWLEDGEMENTS

The authors acknowledge with thanks the financial support of the National Natural Science Foundation of China (Grant No. 10671157), the Natural Science Foundations of Ningxia, China (Grant No. 2006241), the Scientific Research Program of Institutions of Higher Educations of Ningxia, China (under Grant No. 2006JY016), the Ministry of Education of China, and the University of Aberdeen.

REFERENCES

1. Kang H, Choi SU. Reynolds stress modeling of rectangular open-channel flow. *International Journal for Numerical Methods in Fluids* 2006; **51**:1319–1334.
2. Rameshwaran P, Naden PS. Three-dimensional numerical simulation of compound channel flows. *Journal of Hydraulic Engineering* (ASCE) 2003; **129**:645–652.
3. Kimural I, Hosoda T. A non-linear k–ε model with reliability for prediction of flows around blunt bodies. *International Journal for Numerical Methods in Fluids* 2003; **42**:813–837.
4. Sugiyama H, Hitomi D, Saito T. Numerical analysis of turbulent structure in compound meandering open channel by algebraic Reynolds stress model. *International Journal for Numerical Methods in Fluids* 2006; **51**:791–818.
5. Su X, Li C. Large eddy simulation of free surface turbulent flow in partly vegetated open channels. *International Journal for Numerical Methods in Fluids* 2002; **39**:919–937.
6. Pezzinga G. Velocity distribution in compound channel flows by numerical modeling. *Journal of Hydraulic Engineering* (ASCE) 1994; **120**:1176–1198.

Copyright © 2008 John Wiley & Sons, Ltd.

DOI: 10.1002/fld

7. Cokljat D, Younis BA. Second-order closure study of open channel flows. *Journal of Hydraulic Engineering* (ASCE) 1995; **121**:94–107.
8. Sofialidis D, Prinos P. Compound open-channel flow modeling with nonlinear low-Reynolds k–ε models. *Journal of Hydraulic Engineering* (ASCE) 1998; **124**:253–262.
9. Naot D, Nezu I, Nakagawa H. Hydrodynamic behavior of partly vegetated open channels. *Journal of Hydraulic Engineering* (ASCE) 1996; **122**:625–633.
10. Zhang M, Shen Y, Wu X. 3D Numerical simulation of overbank flow in non-orthogonal curvilinear coordinates. *China Ocean Engineering* 2005; **19**:395–407.
11. Shiono K, Muto Y. Complex flow mechanisms in compound meandering channels with overbank flow. *Journal of Fluid Mechanics* 1993; **376**:221–261.
12. Knight DW, Yuen KWH, Alhamid AAI. Boundary shear stress distributions in open channel flow. In *Physical Mechanisms of Mixing and Transport in the Environment*, Beven K, Chatwin P, Millbank J (eds). Wiley: New York, 1994; 51–87.
13. Naish C, Sellin RHJ. Flow structure in a large scale model of a doubly meandering compound river channel. In *Coherent Flow Structures in Open Channels*, Ashworth PJ, Nennett SJ, Best JL, McLelland SJ (eds). Wiley: New York, 1996; 631–654.
14. Sellin RHJ, Wilson CAME, Naish C. Model and prototype results for a sinuous two-stage river channel design. *Journal of Chartered Institution of Water and Environmental Management* 2001; **13**:207–216.
15. Knight DW, Sellin RHJ. The SERC flood channel facility. *Water and Environment Journal* 1987; **1**:198–204.
16. Knight DW, Shinon K. Turbulence measurements in a shear layer region of a compound channel. *Journal of Hydraulic Research* 1990; **28**:175–196.
17. Shinon K, Knight DW. Turbulent open-channel flows with variable depth across the channel. *Journal of Fluid Mechanics* 1991; **222**:617–646.
18. Mellor GL, Herring HJ. A survey of mean turbulent field closure. *AIAA Journal* 1973; **11**:590–599.
19. Speziale CG, Sarkar S, Gatski T. Modeling the pressure strain correlation of turbulence: an invariant dynamical systems approach. *Journal of Fluid Mechanics* 1991; **227**:245–272.
20. Pantankar SV, Spalding DB. A calculation procedure for heat, mass and momentum transfer in three-dimensional parabolic flows. *International Journal of Heat and Mass Transfer* 1972; **15**:1787–1806.
21. Fletcher CAJ. *Computational Technique for Fluid Dynamics.* Springer: Berlin, 1991.
22. Launder BE, Spalding DB. The numerical computation of turbulent flows. *Computer Methods in Applied Mechanics and Engineering* 1974; **3**:269–289.
23. Celik I, Rodi W. Modeling suspended sediment transport in non-equilibrium situation. *Journal of Hydraulic Engineering* (ASCE) 1988; **114**:1157–1191.

Copyright © 2008 John Wiley & Sons, Ltd.

DOI: 10.1002/fld